A Low-Frequency Dual-Band Operational Microphone Mimicking the Hearing Property of *Ormia Ochracea*

Yansheng Zhang, Ralf Bauer, *Member, IEEE*, Joseph C. Jackson, William M. Whitmer, James F. C. Windmill, *Senior Member, IEEE*, and Deepak Uttamchandani, *Senior Member, IEEE*

***Abstract*— This paper introduces a directional MEMS microphone designed for hearing aid applications appropriate to low-frequency hearing impairment, inspired by the hearing mechanism of a fly, the female *Ormia ochracea*. It uses both piezoelectric and capacitive sensing schemes. In order to obtain a high sensitivity at low frequency bands, the presented microphone is designed to have two resonance frequencies below the threshold of low-frequency hearing loss at approximately 2 kHz. One is around 500 Hz and the other is slightly above 2 kHz. The novel dual sensing mechanism allows for optimization of the microphone sensitivity at both frequencies, with a maximum open-circuit (excluding pre-amplification) acoustic response captured via differential piezoelectric sensing at approximately −46 dB (V) ref. 94 dB (SPL) at the resonance frequencies. The corresponding minimum detectable sound pressure level is just below −12 dB. The comb finger capacitive sensing was employed due to a lower electrical response generated from a ground referenced single-ended output by the piezoelectric sensing at the first resonance frequency compared with the second resonance frequency. The capacitive sensing mechanism, connected to a charge amplifier, generates a −28.4 dB (V) ref. 94 dB (SPL) acoustic response when the device is excited at either of the two resonance frequencies. Due to the asymmetric geometry and the 400 μm thick substrate, the device is predicted to perform as a bi-directional microphone below 3 kHz, which is shown by the measured directional polar patterns. [2018-0036]**

***Index Terms*— Low frequency acoustics, microphone, biologically inspired, *Ormia ochracea*, dual-band.**

I. Introduction

SINCE Knowles released the first commercial MEMS microphone – SiSonic in 2001, MEMS microphones have been widely used in mobile applications such as smartphones, laptops, hearing aids, digital assistants, etc. due to their extremely small footprint, high signal to noise ratio and lower power consumption compared to traditional electret condenser microphones. Most MEMS microphones can be categorized into two types: omnidirectional and unidirectional. When surrounding environmental noise cancellation is of the greatest consideration in an application's development such as in vocal device and live recordings, unidirectional microphones are the first choice for developers. Instead of generating an electrical response from acoustic energy arriving from all directions around the device, as the omnidirectional microphone does, the unidirectional microphone has its strongest output when acoustical energy arrives along a single axis vertical through or parallel with the surface of a vibrational membrane. The omnidirectional and the unidirectional MEMS microphones also have different frequency response patterns. In order to achieve a flat response in the frequency range of interest, and also due to their miniature scale, the resonance frequencies of both types of microphones' membranes are set much higher than the maximum working frequencies. As the omnidirectional microphones (most of them are condenser type microphones) enclose an air cavity between the membrane and the electrode on a back plate, air damping is introduced into the system and decreases the Q factor, extending the bandwidth and flattening the frequency response below the resonance frequency. However, the membranes of most commercial unidirectional MEMS microphones are exposed to the medium to create pressure gradient between the front and the rear of the vibrational membrane. This open geometry reduces air damping and provides a higher Q factor, therefore most unidirectional MEMS microphones work as a high-pass filter throughout the frequency range of interest and do not have a strong response at low frequency bands. To resolve this shortcoming in the unidirectional microphones, researchers have found several solutions [1]–[3]. One option is to combine two identical omnidirectional MEMS microphones into an array and utilize the time difference of sound arrival (TDOA) between the two elements in order to derive the sound incident angle. Nonetheless, the whole package size of this solution is at least twice the size of a single MEMS microphone, and any mismatch between the two microphones can introduce localizing errors.

Manuscript received February 23, 2018; revised May 11, 2018; accepted June 3, 2018. This work was supported in part by the EPSRC under Grant EP/M026701/1 and in part by the European Research Council through the European Union's Seventh Framework Programme under Grant FP/2007-2013 and ERC under Grant 615030. Subject Editor C. Rembe. *(Corresponding author: Yansheng Zhang.)*

Y. Zhang, R. Bauer, J. C. Jackson, J. F. C. Windmill, and D. Uttamchandani are with the Department of Electronic and Electrical Engineering, University of Strathclyde, Glasgow G1 1XW, U.K. (e-mail: yansheng.zhang.101@strath.ac.uk; ralf.bauer@strath.ac.uk; joseph.jackson@strath.ac.uk; james.windmill@strath.ac.uk; d.uttamchandani@strath.ac.uk).

W. M. Whitmer is with the Scottish Section, Medical Research Council/Chief Scientist Office Institute of Hearing Research, Glasgow G31 2ER, U.K. (e-mail: bill.whitmer@nottingham.ac.uk).

Color versions of one or more of the figures in this paper are available online at http://ieeexplore.ieee.org.

Digital Object Identifier 10.1109/JMEMS.2018.2845680

In 2002, Tan *et al.* [4] built a biomimetic directional MEMS microphone structure based on their previous research, Miles *et al.* [5], on the hearing mechanism of a female parasitoid fly, the *Ormia ochracea*. This species of fly is able to detect the 5 kHz mating calls of their cricket host with a 2-degree resolution relying on two tympana only separated by 500 μm underneath the insect's head. The mechanical coupling generated by an intertympanal bridge connecting the two tympana enhances the mechanical sensitivity and increases the TDOA. Moreover, the hearing organ working at its two main mode shapes – rocking mode (i.e. two membranes moving out of phase) and bending mode (i.e. two membranes moving in phase) generated by the mechanical coupling can be regarded as a pressure gradient microphone (i.e. a unidirectional microphone) and a pressure microphone (i.e. an omnidirectional microphone), respectively. Further, the hearing organ performs as a combination of these two basic microphone models. In the years following the initial publications, R. Miles's research group developed various MEMS microphones mimicking the mechanical performance of *Ormia*'s hearing organ, integrated with different sensing methods [6], [7] and having different geometrical size [8], [9]. The basic model of the design is constructed with a fully released polysilicon plate and a T-shaped torsional beam placed at its center, orthogonal to the plate's long axis. The torsional beam not only works as a pivot allowing the model to perform a see-saw rocking mode, but also divides the plate into two diaphragms with the same surface area that represents the two identical tympana of the fly *Ormia*, and hence include a bending movement mode shape. The frequency response of their latest device resembles a narrow band-pass filter with the first resonance frequency ($\sim$400 Hz) as the central frequency [10]. Other research groups have also studied the *Ormia*-inspired MEMS microphones. Liu *et al.* [11] established an optical sensing microphone with two clamped circular membranes, working at 8 kHz based on TDOA measurement. Ono *et al.* [12] and Chen and Cheng [13] also studied the microphone working in two dimensions and built centrally supported models. Touse *et al.* [14] designed the first simultaneously dual-band operational microphone structure but with no electrical measurement reported. Kuntzman *et al.* [15] developed a PZT sensing microphone with the first resonance frequencies at 13 kHz. In addition to the works mentioned, the authors' research group has also developed several *Ormia*-inspired piezoelectric dual-plate microphones operating in multiple frequency bands [16], [17].

Previous studies have demonstrated various microphone applications from audio to ultrasonic bands. The research in this paper concentrates on designing an *Ormia*-inspired directional MEMS microphone for hearing aids used by low frequency (or reverse-slope) hearing loss patients, which has enhanced sensitivity and obvious directional patterns in the low frequency audio range. With low frequency hearing loss, people are generally unable to hear at frequencies below 2 kHz. Unlike most patients with high frequency hearing loss, low hearing loss patients can clarify the pitch of words and sentences, so they are more comfortable in individual conversation. However, they usually have difficulty of hearing in group conversations and in noisy environments. As low frequency impairment is much rarer than the high frequency hearing loss, the hearing aids for low frequency hearing impairment are typically those pre-designed for high frequency loss and do not offer a complete resolution of the hearing problem. Compared to previously mentioned designs, the present work moves the bending resonance frequency close to 2 kHz by lateral shifting the torsional beam, thus changing the mass ratio of the two diaphragms. The design however still keeps the fundamental resonance mode shapes as shown in Fig. 1 and unifies the directional behavior of the device at the two main resonance frequencies, which broadens the low frequency response. The piezoelectric sensing film covers the area of the vibrating membrane with high strain to produce sensing elements. As there is no charge pump, as is utilized in a condenser microphone and consumes time before the device reaches the steady-state, the piezoelectric microphone has a faster transient response just after powering it on compared to the condenser microphone. This paper also discusses the impacts of the bias of torsional beam to the center of the whole vibrational plate and varying substrate thickness on the frequency response and the directional patterns of the *Ormia*-inspired microphone as well as the pressure field surrounding the device.

II. Design and Analytical Model

Unlike the *Ormia*-inspired MEMS microphones that have traditional symmetric geometry (i.e. the shape and the mass of the two diaphragms are identical), the biomimetic MEMS microphone presented here is designed with asymmetric geometry (see Fig. 1). The device is fabricated with PiezoMUMPs, a multi-user MEMS foundry service based on single crystal silicon (SCS) provided by MEMSCAP. The device is constructed with two vibrational diaphragms of 10 μm thickness, which are linked to a 30 μm width serpentine torsional beam by a 70 μm $\times$ 5 μm bridge at the center of the torsional beam and two 400 μm $\times$ 20 μm beams that enhance the mechanical coupling between the two diaphragms and reduce the impact of a twisting motion on low frequency performance. The serpentine springs keep the first resonance frequency at a comparably low value, which compensates for the otherwise present high resonance frequency due to the thicker single-crystal silicon device layer (compared to polysilicon) used in the MEMSCAP process. The surface area of the larger diaphragm is around 1.83 mm^2 while the area of the smaller diaphragm is approximately 1.03 mm^2. The torsional beam is fixed to a 400 μm thick silicon-on-insulator (SOI) substrate with an open backside. In addition, two rows of 100μm $\times$ 5μm comb fingers with 5 μm gaps are connected to the ends of the two diaphragms, combining with two sets of fixed comb fingers to afford an auxiliary sensing method. Including the comb fingers, the entire size of the activating area is 3.2 mm $\times$ 1.42 mm. A 500 nm thick Aluminum Nitride (AlN) piezoelectric layer is deposited on the region of the device that is close to the torsional beam.

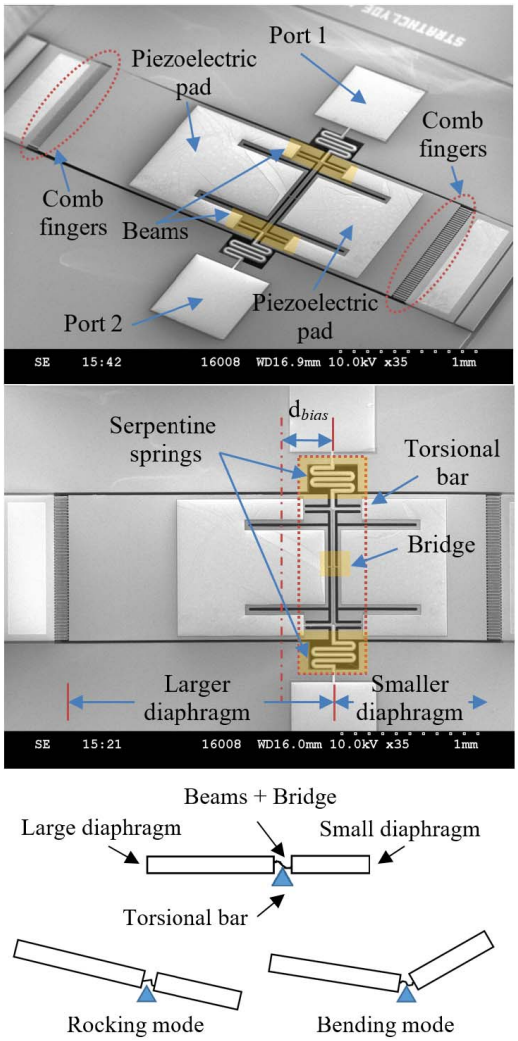

Fig. 1. Scanning Electron Microscope (SEM) images of the presented asymmetric *Ormia*-inspired MEMS microphone and the schematic of its resonance mode shapes.

The voltage potential generated by the AlN layer is then transferred to the output ports via 20 nm Cr and 1 μm Al composite metal layers attached on the piezoelectric layer and the oxide layer covering the torsional beam.

A. Analytical Model

The mechanical vibration model of *Ormia ochracea*'s hearing system has previously been reported [5], which assumes that the mass of two tympana are the same as well as the stiffness of the tympana and the damping caused by the air cavity underneath, and thus infers the Eigen-frequencies and mechanical frequency response of the system. These assumptions are also applied in their subsequent symmetric microphone development [18]. In the case of this paper, the mass M of the two diaphragms are different, as well as the distance between the rotation beam and each diaphragm centroid. Fig. 2 shows the two-degree-of-freedom equivalent mechanical vibration model of the design. Leaving the air damping between the comb fingers out of consideration,

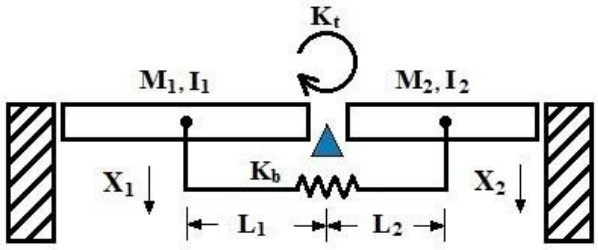

Fig. 2. The equivalent mechanical vibration model for the design.

the equations of motion in the frequency domain can be expressed as

$$I\ddot{\theta}(\omega) + K_t\theta(\omega) = F_1(\omega)L_1 - F_2(\omega)L_2, \tag{1}$$

$$\begin{bmatrix} -\alpha M\omega^2 & 0 \\ 0 & -M\omega^2 \end{bmatrix}\begin{bmatrix} \ddot{X_1}(\omega) \\ \ddot{X_2}(\omega) \end{bmatrix} + \begin{bmatrix} K_b & K_b \\ K_b & K_b \end{bmatrix}\begin{bmatrix} X_1(\omega) \\ X_2(\omega) \end{bmatrix} = \begin{bmatrix} F_1(\omega) \\ F_2(\omega) \end{bmatrix} \tag{2}$$

where $M = M_2 = 2.37 \times 10^{-8}$ kg and $\alpha = \frac{M_1}{M_2} = 1.774$; K_t is the torsional stiffness of the rotation beam; K_b is the total bending stiffness of the bridges; I is the mass moment of inertia of the entire plate about the rotation beam; L is the distance between the centroid of each diaphragm and the rotation beam; ω is the driving frequency; $\theta(\omega)$ and $X(\omega)$ represent the angular displacement about the rotation beam and the mechanical displacement after Fourier transform; $F(\omega)$ is the effective forces placed on the diaphragms in frequency domain. The subscripts 1 and 2 represent the diaphragm with larger mass and the diaphragm with smaller mass, respectively. The angular displacement and the mechanical displacement are then given by

$$\theta(\omega) = \frac{F_1(\omega)L_1 - F_2(\omega)L_2}{I(\omega_r^2 - \omega^2)}, \tag{3}$$

$$X_1(\omega) = \frac{F_1(\omega)\left(M\omega^2 - K_b\right) + F_2(\omega)K_b}{\alpha M^2\omega^2\left(\omega_b^2 - \omega^2\right)}, \tag{4}$$

$$X_2(\omega) = \frac{F_2(\omega)\left(\alpha M\omega^2 - K_b\right) + F_1(\omega)K_b}{\alpha M^2\omega^2\left(\omega_b^2 - \omega^2\right)}, \tag{5}$$

where ω_r and ω_b are the eigen-frequencies of the rocking and bending modes, respectively, that can be expressed as

$$\omega_r = \sqrt{\frac{K_t}{I}}, \quad \omega_b = \sqrt{\frac{(1+\alpha)K_b}{\alpha M}}. \tag{6}$$

In Eq. 6, the total mass moment of inertia is $I = 6.35 \times 10^{-14}$ kg $\cdot$ m^2. According to G. Barillaro et al.'s work relative to the torsional stiffness of serpentine springs [19], if it is assumed that the length of the folds is much shorter than the length of the spring element l_s parallel to the longitudinal of the membranes as shown in Fig. 3, and neglecting the influence of round corner, we can obtain

$$K_t = 2 \times \left[\frac{48l_s}{Ewt^3} + \frac{2(l_{t1} + 2l_{t2})}{GJ_t}\right]^{-1}, \tag{7}$$

$$J_t = wt^3\left[\frac{16}{3} - 3.36\frac{t}{w}\left(1 - \frac{t^4}{12w^4}\right)\right], \tag{8}$$

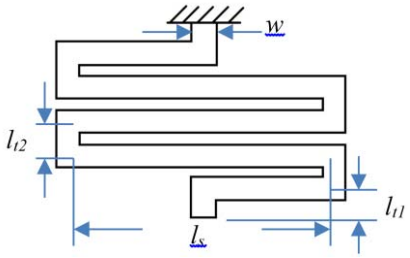

Fig. 3. The schematic of the serpentine springs.

where J_t is the torsion constant of the vertical beams. Substituting the Young's modulus E of SCS (169 GPa), the shear modulus G = 66 GPa, the width of the spring element $w = 30\ \mu m$, the thickness of the spring $t = 10\ \mu m$, $l_{t1} = 25\ \mu$m, $l_{t2} = 40\ \mu$m and $l_s = 280\ \mu$m, then the analytical Eigen-frequency of the rocking mode $f_r = \frac{\omega_r}{2\pi} =$ 511 Hz. The bending stiffness K_b is obtained by a deflection study against load using COMSOL Multiphysics finite element modelling, and is found to be 4.3 N/m. Therefore, the analytical eigen-frequency of the bending mode $f_b = 2.6$ kHz.

Since the mechanical vibration model is regarded as a system of particles, the mass moment of inertia of each diaphragm is relative to the mass concentrating on its center of mass, i.e. $I_1 = L_1^2 M_1$ and $I_2 = L_2^2 M_2$. As the total mechanical response at the centroid of each diaphragm is the superposition of the two main modes shapes, Equation (3), (4), and (5) enable the total displacement $x(\omega)$ to be written as

$$\begin{aligned} x_1(\omega) &= X_1(\omega) + \theta(\omega) L_1 \\ &= \frac{\left[\frac{F_1(\omega)}{\alpha} + \frac{F_2(\omega)-F_1(\omega)}{\Omega^2(1+\alpha)}\right]/M}{\omega_b^2 - \omega^2} + \frac{\frac{\beta[F_1(\omega)\beta - F_2(\omega)]}{M(\beta^2\alpha+1)}}{\omega_r^2 - \omega^2}, \end{aligned} \quad (9)$$

$$\begin{aligned} x_2(\omega) &= X_2(\omega) - \theta(\omega) L_2 \\ &= \frac{\left[F_2(\omega) + \frac{F_1(\omega)-F_2(\omega)}{\Omega^2(1+\alpha)}\right]/M}{\omega_b^2 - \omega^2} - \frac{\frac{F_1(\omega)\beta - F_2(\omega)}{M(\beta^2\alpha+1)}}{\omega_r^2 - \omega^2}, \end{aligned} \quad (10)$$

where $\beta = \frac{L_1}{L_2}$ and $\Omega = \frac{\omega}{\omega_b}$.

When $\alpha = \beta$, Equation (7) and (8) can be simplified and shown as

$$\begin{aligned} x_1(\omega) = &\frac{\left[\frac{F_1(\omega)}{\alpha} + \frac{F_2(\omega)-F_1(\omega)}{\Omega^2(1+\alpha)}\right]/M}{\omega_b^2 - \omega^2} \\ &+ \frac{\left[\frac{\alpha}{\alpha^3+1}(\alpha F_1(\omega) - F_2(\omega))\right]/M}{\omega_r^2 - \omega^2}, \end{aligned} \quad (11)$$

$$\begin{aligned} x_2(\omega) = &\frac{\left[F_2(\omega) + \frac{F_1(\omega)-F_2(\omega)}{\Omega^2(1+\alpha)}\right]/M}{\omega_b^2 - \omega^2} \\ &+ \frac{\left[\frac{1}{\alpha^3+1}(\alpha F_1(\omega) - F_2(\omega))\right]/M}{\omega_r^2 - \omega^2}. \end{aligned} \quad (12)$$

In this case, if the driving frequency is close to the 1st resonance frequency (i.e. $\omega \approx \omega_r$), as most kinetic energy concentrates on the torsional serpentine springs, the displacement amplitude of two diaphragms A_{r1} and A_{r2} has the following relationship,

$$A_{r1} = \alpha A_{r2} \propto |\alpha F_1(\omega) - F_2(\omega)|. \quad (13)$$

When the driving frequency continuously increases and finally approaches the 2nd resonance frequency (i.e. $\omega \approx \omega_t$), most of the kinetic energy transfers from the torsional springs to the bending bridges. The amplitude of the two diaphragms A_{b1} and A_{b2} in this situation are linearly related and can be expressed as

$$A_{b1} = \frac{1}{\alpha} A_{b2} \propto |F_1(\omega) + \alpha F_2(\omega)|. \quad (14)$$

Through (13) and (14), it is apparent that the displacement amplitude of the diaphragms heavily depends on two main factors: the sound pressure field acting on the diaphragms and the ratio of masses. The former factor is relative to the sound pressure gradient between the front and back surfaces of the diaphragms that is influenced by the structure of the substrate in this case. The latter is associated with the bias of the torsional serpentine to the center of the entire active device. The next section will discuss the impact of these two factors on the directional behavior of the device.

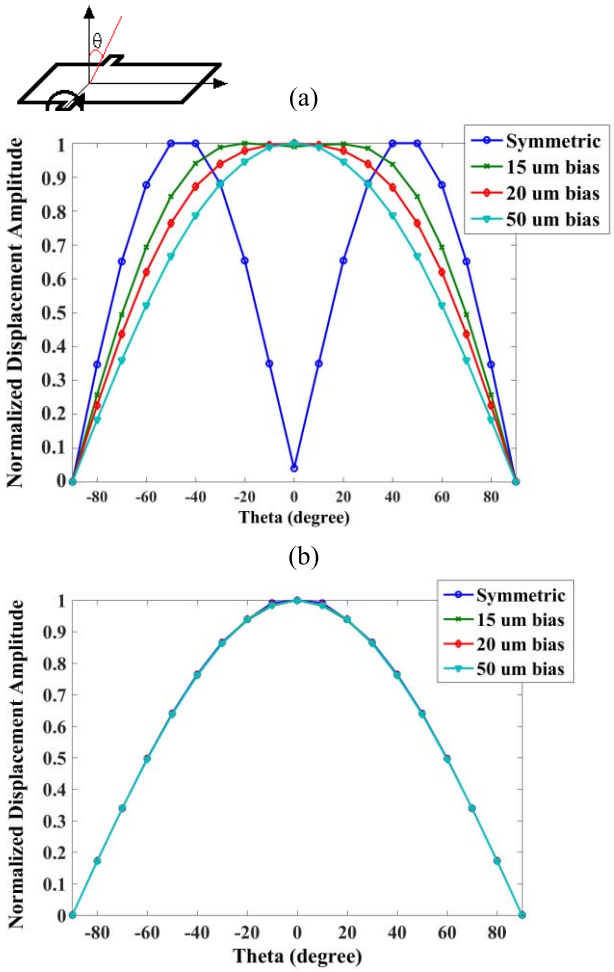

Fig. 4. Directionality of the device with a 10 μm thick substrate when $d_{bias} = 0\ \mu$m, 15 μm, 20 μm, and 50 μm at (a) The 1st resonance frequency and (b) The 2nd resonance frequency.

B. The Impact of the Substrate and the Bias Torsional Beam on Directionality

To investigate the two main factors that influence the directionality of an *Ormia*-inspired MEMS microphone with a see-saw structure, a simplified model is built and simulated in COMSOL using the Acoustic-Solid module. It consists of a single rectangular plate with the same size as the presented device and a rectangular torsional bar that fixes the plate to an open backside substrate. The bottom side of the substrate is assumed to be attached onto a 20 mm × 10 mm × 1.6 mm rigid PCB with a backside hole of 2.25 mm radius, simulating the device under later experimental conditions. The entire model is surrounded by a spherical air domain covered by an acoustic perfect matching layer. A 1 Pa plane wave is applied in the air domain. First of all, it is assumed that the substrate is as thick as the diaphragms and the dimensions of the see-saw *Ormia*-inspired MEMS microphone are a constant. By changing the bias value of the torsional beam d_{bias} relative to the center of the plate, the variation of the displacement amplitude of the device against the sound incident angle θ at the 1st and the 2nd resonance frequencies are obtained as illustrated in Fig. 4(a) and 4(b). As can be seen in Fig. 4(a), the displacement amplitude of the plate excited at the 1st resonance frequency is proportional to $|\sin 2\theta|$ when the device is symmetric. When increasing d_{bias}, the displacement amplitude gradually turns to a cosine function of the sound incident angle. However, the bias of the torsional beam does not affect the directional behavior of the model at the 2nd resonance frequency, which remains as a cosine function of the sound incident angle.

Secondly, in order to study the relationship between the thickness of the substrate and the directionality, the model is initially regarded as symmetric. When the thickness of the substrate increases from 10 μm to 400 μm, the displacement amplitude of the model at the 1st resonance mode changes from a $|\sin 2\theta|$ function to a function similar to $|\sin\theta|$, while it stays as a cosine function of θ at the 2nd resonance mode (see Figure 5(a)). However, the directionality of the simplified model with a somewhat larger d_{bias}, such as 300 μm is independent of the thickness of the substrate and the driving frequency as shown in Fig. 5(b). In terms of the final presented device which has a torsional beam with nearly 400 μm bias relative to the central and a 400 μm thick substrate, its directional behavior is predicted as that in the plot in Fig. 5(b).

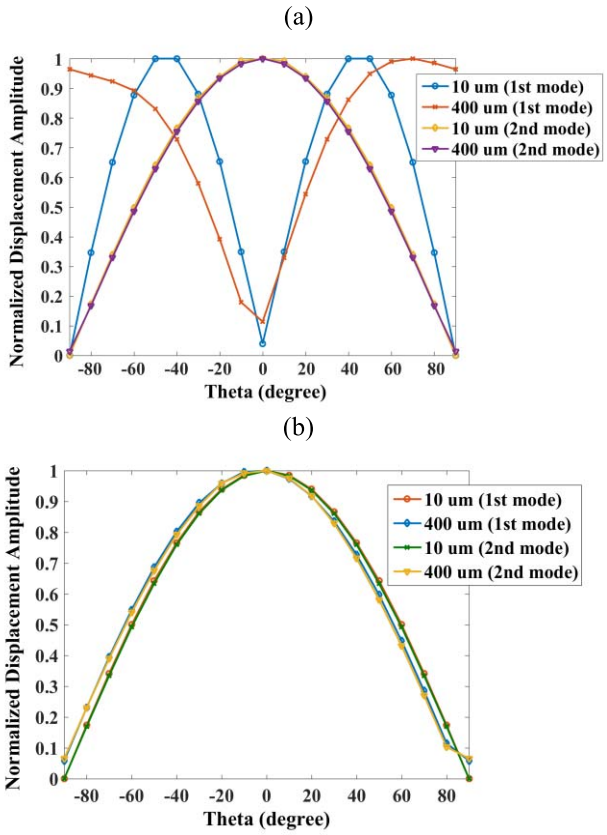

Fig. 5. Directionality of the device with a 10 μm or 400 μm thick substrate at the 1st and the 2nd resonance frequencies when d_{bias} equals to (a) 10 μm (b) 300 μm.

III. Readout Circuit and Experimental Setup

As the piezoelectric cantilevers are placed close to the torsional beam, the strain occurring on the cantilevers driven around the resonance frequency of the rocking mode is much smaller than that when driven around the resonance frequency of the bending mode so that the charge generated by the piezoelectric material at the rocking mode is expected to be lower than at the bending mode. Therefore, the capacitive comb finger sensing scheme is introduced as an auxiliary sensing element for the device since the variation of the capacitance is linear to the displacement of the diaphragms. However, since the piezoelectric sensor does not require a bias voltage as the capacitive sensing does, the sensing process neither generates electrostatics force that drags on the sensitivity of the diaphragms nor produces an unstable output due to the battery loss. The two sensing methods are two separated systems so that there is no cross-talk phenomenon during the measurements.

A. Readout Circuit for Piezoelectric Sensing

When a force deforms the piezoelectric material, both charge and voltage are generated at the same time. Generally, the output of a piezoelectric sensor is amplified by a charge amplifier as the output stage of the amplifier is not influenced by the capacitance associated with the interfacing cable between the output stage of the sensor and the input stage of the amplifier. The feedback resistor and capacitor of the charge amplifier apply a high-pass filter to the output signals, which is not a critical problem for high frequency applications such as ultrasonic transducers but an important consideration for audio applications. As the gain is inversely proportional to the feedback capacitance of the circuit and the feedback capacitance is also inversely proportional to the feedback resistor for a fixed cut-off frequency, the feedback resistor is proportional to the output gain. Thus, in order to achieve a large output gain, the feedback resistor has to be set as high as possible, which then results in a stronger thermal noise so reducing the SNR.

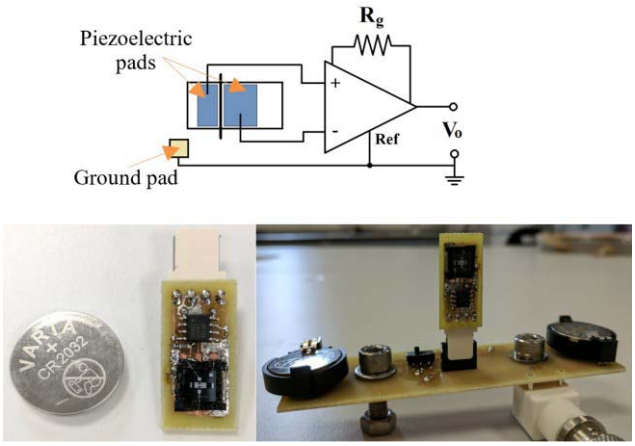

Fig. 6. The readout circuit for piezoelectric sensing. The die is wire-bonded on the frontal surface of the PCB whereas the readout circuit is soldered just beside.

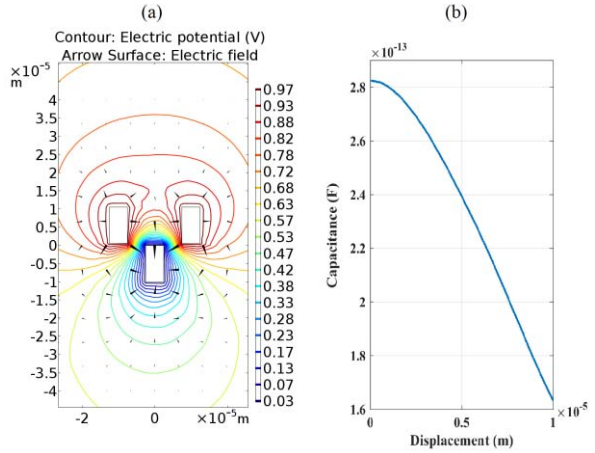

Fig. 7. Analysis of capacitive sensing of the device: (a) The electric field between a unit of capacitive comb fingers where the bias voltage is 1V; (b) The simulated total capacitance of a set of comb fingers. The capacitance at the initial stage is expected to be $2.83 \times 10^{-15} F$.

The alternative amplification method for this case is using an instrumentation amplifier. The instrumentation amplifier has two initial buffers at the input stage of the amplifier, followed by a differential amplifier with high common-mode rejection ratio (CMRR). The buffers match the high output impedance of the piezoelectric sensor with the input impedance of the subsequent differential amplifier to obtain maximum output voltage from the sensor. The output gain is only controlled by a gain resistor R_g as shown in Fig. 6. Additional filters can be applied to the output stage of the amplifier for further post processing. For measuring the device presented in this work, the instrumentation amplifier INA141 with $Gain = 100$ is utilized. The measured output voltage of the piezoelectric sensing is

$$V_{op}(\omega) = Gain \times \left(H_{vx1}(\omega) \times x_1(\omega) - H_{vx2}(\omega) \times x_2(\omega)\right), \tag{15}$$

where H_{vx1} and H_{vx2} are the transfer functions between the open-circuit voltage at the output stage of the piezoelectric ports corresponding to the large diaphragm and the small diaphragm, respectively, to their deflection. The differential output cancels the common-mode noise from the two piezoelectric ports.

B. Readout Circuit for Capacitive Sensing (Auxiliary)

The total capacitance between the comb fingers is the sum of the capacitance between two neighboring fingers and the capacitance between the tips of the comb fingers and the beam. Figure 7 demonstrates the electric field between one unit of comb fingers and the total simulated capacitance against diaphragm displacement, simulated by COMSOL. The intrinsic stress and thermal stress due to the fabrication causes a 4.8 μm initial offset between the pair of fingers. Therefore, as shown in Fig. 7(b), the capacitance of this set of comb fingers is linear over the deflection of the diaphragm. The variation of the capacitance is converted to the voltage output signal by using a charge amplifier with a feedback capacitor $C_f = 1\ pF$ and a feedback resistor $R_f = 10\ M\Omega$ as shown

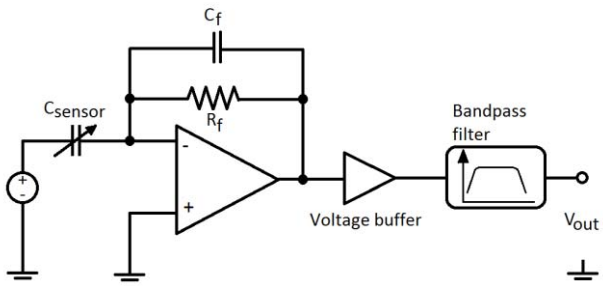

Fig. 8. Schematic of readout circuit for capacitive sensing.

in Fig. 8. The amplified signal is then filtered by a 4th order band-pass filter. Although the device has two separate sets of comb fingers for the larger diaphragm and the smaller diaphragm, the initial curvature of the larger diaphragm is about 0.1 m which brings a 15.3 μm offset relative to the upper surface of the fixed finger, hence it does not provide sufficient overlapped area between the fingers and causes extremely low initial capacitance. This is mainly due to the inherent stress built by the piezoelectric and SCS layers. Therefore, the capacitive finger set for the larger diaphragm was not tested during experiments. The output voltage at the output stage of the charge amplifier for the capacitive sensing

$$V_c(\omega) = \frac{V_{bias}}{C_f} \times \frac{dC_{sensor}(\omega)}{dx(\omega)} |x(\omega), \tag{16}$$

where V_{bias} is the bias voltage in the charge amplifier circuit (5 V for this application) and $C_{sensor}(\omega)$ is the total capacitance of the comb fingers in the frequency domain.

C. Experimental Setup

The resonance mode shapes of the fabricated device are confirmed by a Polytec PSV-300-F laser Doppler vibrometer (LDV) with scanning head OFV-056. The experimental

TABLE I

COMPARISON BETWEEN THE EVALUATED EIGENFREQUENCIES AND THE EIGENFREQUENCIES MEASURED BY LDV

	The 1st mode (Hz)	The 2nd mode (Hz)
Analytical model	511	2600
COMSOL simulated	466	2532
LDV	464	2275

setup for measuring the acoustic response from the piezoelectric ports is similar to that in [18]. Except here both the die and the preamplifier are wire-bonded and soldered onto the same printed circuit board which is directly connected to a 6 V (±3V) battery stage providing the power to the preamplifier through a board-to-board connector as shown in Fig. 6. The battery stage includes the BNC output. The electrical signal v from the capacitive ports is amplified by a separated charge amplifier. The output signal acquired using either sensing methods is captured by a SR850 lock-in amplifier before being sampled by a computer.

Furthermore, the battery stage is fixed onto an automatic rotation stage driven by a step motor controlled by a PC. This allows the relative sound incident angle to be changed when measuring the directional polar patterns of the device. A commercial omni-directional MEMS microphone, InvenSense INMP411, and a unidirectional MEMS microphone, Knowles TD24621, are utilized as angular reference microphones for the directionality measurements using the same experimental setup.

IV. EXPERIMENTAL RESULTS

A. Frequency Response

The first two resonance frequencies measured by LDV are about 464 Hz and 2275 Hz, which is only slightly lower than the results calculated from the lumped model and the COMSOL simulation. This is most likely due to the omission of the metal layers deposited on the piezoelectric material and the metal path on the bending bridges in the simulation. Table I compares the evaluated Eigenfrequencies with the experimental results. As shown in Fig. 9, the two diaphragms of the device vibrate out-of-plane at the 1st resonance frequency and then move in-plane at the 2nd resonance frequency, closely matching with expectations. Figure 9 also gives the differential acoustic frequency spectrum of the device obtained through the piezoelectric sensors below 3 kHz. Taking no account of pre-amplification, the measured open-circuit acoustic response through the piezoelectric units is 3.6 mV/Pa at the 1st resonance frequency and then jumps to the maximum output response of 4.9 mV/Pa (i.e. – 46 dB (V) ref. 94 dB (SPL)) when the device is excited at the 2nd resonance frequency. The Q factors at these two resonance frequencies equal to 31 and 28, respectively. The experimental acoustical response measured by the piezoelectric sensing units are closely matched with the COMSOL simulation.

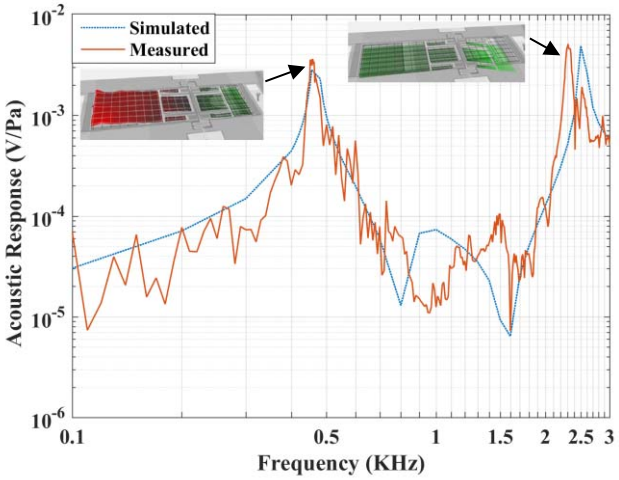

Fig. 9. The resonance mode shapes of the device and its differential acoustic frequency response sensed via piezoelectric material.

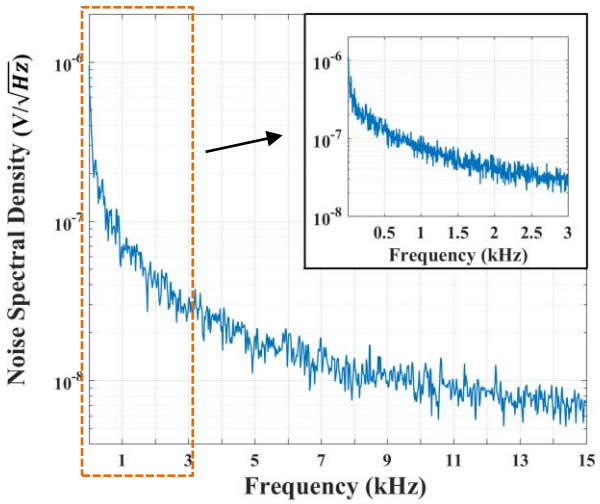

Fig. 10. The noise floor of the prototype when capturing signals from piezoelectric material, including the input voltage and current noise of the instrumentation preamplifier.

The noise spectral density at the input end of the preamplifier when using the piezoelectric sensing units is also measured with an Agilent 4365A spectrum analyzer, which is plotted in Fig. 10. Due to the high input impedance of the instrumentation amplifier, two high value resistors (usually over 10 kΩ) are required to be connected between the inputs and ground in order to create bias current paths and prevent output saturation when measuring the differential signals, which introduces a large amount of Johnson noise into the system. In addition, for a piezoelectric sensor, another dominant noise source stems from the dielectric loss of the piezoelectric material [16] which is controlled by the fabrication process. The noise around 500 Hz and 2.3 kHz is about 0.15 $\mu V/\sqrt{\text{Hz}}$ and 0.025 μ V$/\sqrt{\text{Hz}}$, respectively, whereas the input voltage noise of the preamplifier is about 8 nV$/\sqrt{\text{Hz}}$ from 100 Hz according to the datasheet. The average noise density of the

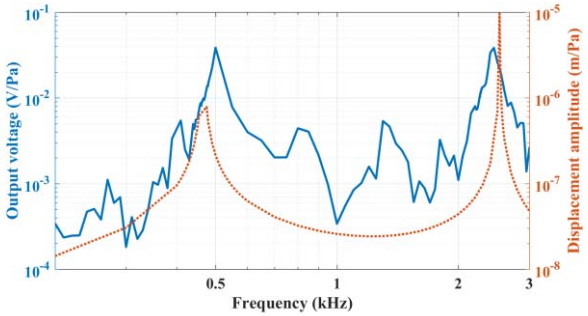

Fig. 11. The acoustic response measured via capacitive comb fingers, compared to the simulated mechanical response of the small diaphragm of the device.

prototype below 3 kHz is about 0.087 $\mu V/\sqrt{Hz}$. Therefore, the minimum detectable sound pressure around the 1st resonance frequency is approximately 6.38 dB (SPL) and this value reduces to −12.04 dB (SPL) around the 2nd resonance frequency.

When acquiring an electrical signal from the capacitive port sensing the deflection of the small diaphragm, we obtain an acoustic response which is similar to the acoustic response captured from the piezoelectric ports and the simulated mechanical response of the diaphragm as shown in Fig. 11. The acoustic response at both the 1st and the 2nd resonance frequencies is approximately 38 mV/Pa (i.e. −28.4 dB (V) ref. 94 dB (SPL)). As the charge amplifier has a built-in band-pass filter, this measured acoustic response takes amplification into account and has more attenuation around the first resonance frequency. The capacitive sensing is an auxiliary sensing method, and only the deformation of the small diaphragm could be detectable at this stage, thus this aspect will be investigated further in the future. Although the results demonstrated in Fig. 11 do not show that the capacitive sensing unit linked to the smaller diaphragm brings a higher acoustic response at the rocking mode than at the bending mode, it can be derived that a differential output of capacitive sensing could provide higher response at lower resonance frequency through (13) and (14).

B. Directionality

A directional polar pattern is a critical specification to confirm the directionality of the device. Figure 12 (a) shows the directional polar patterns of this device in the plane that is normal to the diaphragms, obtained through the piezoelectric ports at the resonance frequencies and their nearby frequencies. At the resonance frequencies, the measured polar patterns are close to typical figure-8 patterns as expected from the analytical model where the diaphragm transfers the greatest portion of sound energy into mechanical deflection when sound waves are vertically incident onto its front surface. For driving frequencies off the main resonance below 3 kHz, the device gives a slightly unbalanced response between the front and the back but still has bi-directional polar patterns. Comparing directional polar patterns of the device with the polar patterns of the omnidirectional microphone INMP411, it is obvious that the device can be regarded as a bi-directional

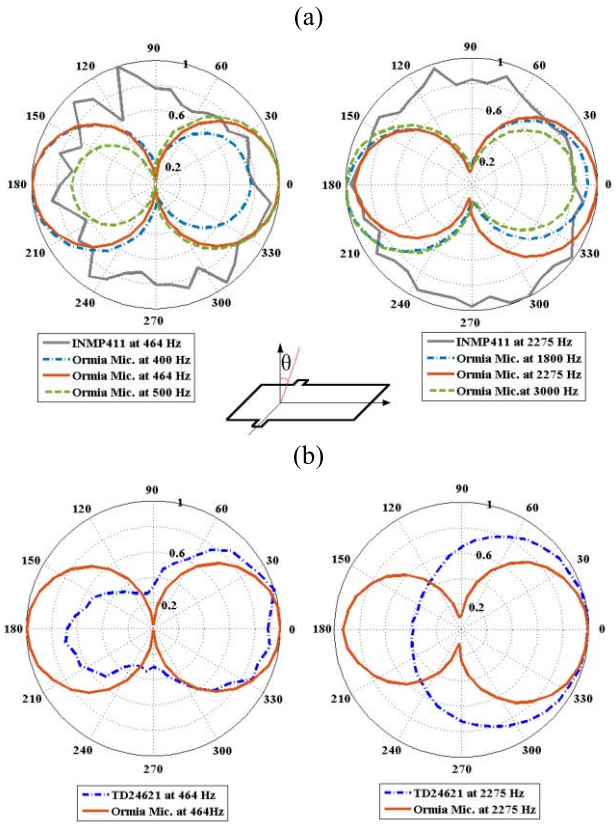

Fig. 12. Directional polar patterns of (a) Omni-directional MEMS microphone INMP411 and *Ormia*-inspired microphone at the resonance frequencies (464 Hz and 2275 Hz) and their nearby frequencies (400 Hz, 500 Hz, 1800 Hz and 3000 Hz); (b) Unidirectional MEMS microphone TD24621 and *Ormia*-inspired microphone at the resonance frequencies.

microphone at least from 400 Hz to 3000 Hz. Meanwhile, comparing the polar patterns of unidirectional microphone TD24621 with the polar patterns of the device at its resonance, the *Ormia*-inspired microphone has much clearer directional behavior than the commercial reference in the low frequency range as shown in Figure 12 (b).

V. Discussion and Conclusion

Most hearing aids are designed for high frequency hearing loss. This leaves limited choices for patients having low frequency impairment. The presented dual-sensing device is designed for this particular purpose, and two mechanisms are used to lower its resonance frequencies. First of all, the T-shape cross-section torsional beam that was applied in previous designs [7] is replaced by a combination of simple rectangular torsional beams and serpentine beams, which reduces the torsional stiffness K_t, thus decreasing the 1st resonance frequency. In addition, the introduction of two thin beams that connect the diaphragms to the torsional bar reduces the bending stiffness K_b so that the 2nd resonance frequency remains at a value in the low kHz range. Both modifications also allow the microphone to be built using a cost-effective multi-user foundry service providing high yield. Moreover, by creating a lateral shift of the position of the torsional beam in the device geometry, the presented device was predicted to

retain the similar bi-directional acoustic response at the two fundamental resonance frequencies as shown in Fig. 4 and Fig. 5. The experimental results agree with the theoretically predicted behavior and reveal that the presented device also achieves a bi-directional acoustic response in the frequency bands off the main resonance frequencies below 3 kHz, which improves the acoustic response especially below 500 Hz where the signal can easily be covered by $1/f$ noise. Finally, the acoustic responses measured through both the piezoelectric sensing and capacitive sensing units of the initial prototype are closely matched with the theoretical predictions.

Future work includes increasing the SNR for piezoelectric sensing and improving the capacitive sensing. In terms of obtaining higher SNR for piezoelectric sensing, it will be achieved by adjusting the structure to increase the strain of the sensing area and modifying the distribution of the piezoelectric material on the diaphragms to reduce the total mass and increase the mechanical sensitivity but not raise the 1st resonance frequencies. The modification of piezoelectric material distribution will also be beneficial to reduce curvature of the large diaphragm and so increase the initial capacitance between the comb fingers. A differential readout will then be applied to capture electric signals from both sets of capacitive sensing units to enhance the response around the low resonance frequency and reduce the common mode noise. The further combination of these two sensing mechanisms will also be studied, which aims to add more functionalities to the device, e.g. users will be able to personally customize the device through digital methods. Furthermore, the stiffness of the bending bridges will be decreased in future devices to reduce the 2nd resonance frequency down to 1-2 kHz so that the overlap between the two bands near the resonances will increase the average acoustic response and the minimum detectable sound pressure, thus allowing the device to be more sensitive to the human vocal range. In addition, a metal-coated package could be built with carefully designed interior sound path for pressure gradient and RF shielded function in the future.

REFERENCES

[1] D. P. Jarrett, E. A. P. Habets, and P. A. Naylor, "Introduction," in *Theory and Applications of Spherical Microphone Array Processing*, vol. 9. Cham, Switzerland: Springer, 2016, pp. 1–10.

[2] D. P. Welker, J. E. Greenberg, J. G. Desloge, and P. M. Zurek, "Microphone-array hearing aids with binaural output. II. A two-microphone adaptive system," *IEEE Trans. Speech Audio Process.*, vol. 5, no. 6, pp. 543–551, Nov. 1997.

[3] S. C. Thompson, "Tutorial on microphone technologies for directional hearing aids," *Hear J.*, vol. 56, no. 11, pp. 14–21, Nov. 2003.

[4] L. Tan *et al.*, "Response of a biologically inspired MEMS differential microphone diaphragm," *Proc. SPIE*, vol. 15, pp. 1–8, Aug. 2002.

[5] R. N. Miles, D. Robert, and R. R. Hoy, "Mechanically coupled ears for directional hearing in the parasitoid fly *Ormia ochracea*," *J. Acoust. Soc. Amer.*, vol. 98, no. 6, pp. 3059–3070, 1995.

[6] R. N. Miles *et al.*, "A low-noise differential microphone inspired by the ears of the parasitoid fly *Ormia ochracea*," *J. Acoust. Soc. Amer.*, vol. 125, no. 4, pp. 2013–2026, 2009.

[7] R. N. Miles, W. Cui, Q. T. Su, and D. Homentcovschi, "A MEMS low-noise sound pressure gradient microphone with capacitive sensing," *J. Microelectromech. Syst.*, vol. 24, no. 1, pp. 241–248, Feb. 2015.

[8] B. Bicen *et al.*, "Integrated optical displacement detection and electrostatic actuation for directional optical microphones with micromachined biomimetic diaphragms," *IEEE Sensors J.*, vol. 9, no. 12, pp. 1933–1941, Dec. 2009.

[9] C. Gibbons and R. N. Miles, "Design of a biomimetic directional microphone diaphragm," *Amer. Soc. Mech. Eng. Noise Control Acoust. Division NCA*, vol. 27, pp. 173–179, Sep. 2000.

[10] R. Miles, "Comparisons of the performance of Knowles hearing aid microphones to that of the Binghamton Ormia-inspired gradient microphone," Binghamton Univ., Binghamton, NY, USA, Sep. 2015, doi: 10.13140/RG.2.2.17566.95043.

[11] H. J. Liu, M. Yu, and X. M. Zhang, "Biomimetic optical directional microphone with structurally coupled diaphragms," *Appl. Phys. Lett.*, vol. 93, no. 24, p. 243902, Dec. 2008.

[12] N. Ono, A. Saito, and S. Ando, "Design and experiments of biomimicry sound source localization sensor with gimbal-supported circular diaphragm," in *Proc. IEEE 12th Int. Conf. Solid-State Sens., Actuators Microsyst.*, Jun. 2003, pp. 935–938.

[13] C.-C. Chen and Y.-T. Cheng, "Physical analysis of a biomimetic microphone with a central-supported (C-S) circular diaphragm for sound source localization," *IEEE Sensors J.*, vol. 12, no. 5, pp. 1504–1512, May 2012.

[14] M. Touse, J. Sinibaldi, and G. Karunasiri, "MEMS directional sound sensor with simultaneous detection of two frequency bands," in *Proc. IEEE Sensors*, Nov. 2010, pp. 2422–2425.

[15] M. L. Kuntzman, J. G. Lee, N. N. Hewa-Kasakarage, D. Kim, and N. A. Hall, "Micromachined piezoelectric microphones with in-plane directivity," *Appl. Phys. Lett.*, vol. 102, no. 5, pp. 10–14, 2013.

[16] Y. Zhang, R. Bauer, J. F. C. Windmill, and D. Uttamchandani, "Multiband asymmetric piezoelectric MEMS microphone inspired by the *Ormia ochracea*," in *Proc. IEEE 29th Int. Conf. Micro Electro Mech. Syst. (MEMS)*, Jan. 2016, pp. 1114–1117.

[17] R. Bauer *et al.*, "Influence of microphone housing on the directional response of piezoelectric MEMS microphones inspired by *Ormia ochracea*," *IEEE Sensors J.*, vol. 17, no. 17, pp. 5529–5536, Sep. 2017.

[18] R. N. Miles, L. Tan, and S. Sundermurthy, "Design of a biologically inspired directional acoustic sensor," Binghamton Univ., Binghamton, NY, USA, Feb. 2002. [Online]. Available: http://www.dtic.mil/get-tr-doc/pdf?AD=ADA409231

[19] G. Barillaro, A. Molfese, A. Nannini, and F. Pieri, "Analysis, simulation and relative performances of two kinds of serpentine springs," *J. Micromech. Microeng.*, vol. 15, no. 4, pp. 736–746, 2005.

Yansheng Zhang received the bachelor's degree from the University of Strathclyde in 2012, where she is currently pursuing the Ph.D. degree with the Department of Electronic and Electrical Engineering. She is currently a Research Assistant with the Department of Electronic and Electrical Engineering, University of Strathclyde. Her research interests are in the field of biologically-inspired MEMS microphone development.

Ralf Bauer (M'17) received the Dipl.Ing. degree in mechatronics from the University of Erlangen-Nuernberg, Germany, in 2010, and the Ph.D. degree from the University of Strathclyde, Glasgow, U.K., in 2013, with a focus on MEMS enabled solid-state lasers.

He is currently a Lecturer and an R.A.Eng. Engineering for Development Research Fellow with the Department of Electronic and Electrical Engineering, University of Strathclyde. His research interests are in the field of MEMS enabled sensors and systems in the area of biomedical sensors, optical systems, and biomedical imaging systems.

Joseph C. Jackson received the M.Sc. degree (Hons.) in physics from Imperial College London in 2003, and the Ph.D. degree in biological sciences from the University of Bristol in 2008. He is currently a Lecturer in electrical and electronic engineering with the Centre for Ultrasonic Engineering, University of Strathclyde. His research interests cover a wide range of subjects, such as the physical basis for hearing, sound production, and reception in biology and engineering, and advanced bio-inspired transducer and signal design.

William M. Whitmer is currently a Senior Investigator Scientist with the Scottish Section, Medical Research Council/Chief Scientist Office Institute of Hearing Research. He has over 19 years of research experience in human psychoacoustics, including research and development within the hearing-aid industry. His research interests range from novel hearing prostheses to ecological validations of patient benefit.

James F. C. Windmill (SM'17) is currently a Professor with the Department of Electronic and Electrical Engineering, University of Strathclyde, Glasgow, U.K. He has over 18 years of research and development experience in the areas of sensors and hearing systems. His research interests are in the field of biologically inspired acoustic systems, from the fundamental biology to various engineering application topics.

Deepak Uttamchandani (SM'05) received the Ph.D. degree from University College London, London, U.K., in 1985, for research in the areas of optical fiber sensors and optical frequency domain reflectometry. He is currently the Head of the Centre for Microsystems and Photonics, University of Strathclyde, Glasgow, U.K. He has also published in the fields of optofluidic devices and optical sensors, including sub-wavelength tip-based Raman spectroscopy, and *in situ* intraocular drug detection systems via optical spectroscopy in the eye. His early research in MEMS concentrated on opto-thermal microresonator sensors and in investigating techniques for MEMS material characterization using micromechanical resonators. His recent research has concentrated on system applications of optical MEMS, including intra-cavity MEMS-based laser systems, MEMS-based directional microphones, and MEMS-based single-pixel imaging systems. In 2014, he organized and chaired the IEEE Optical MEMS and Nanophotonics Conference, Glasgow, U.K.